Permeability evolution in fractured coal — Combining triaxial confinement with X-ray computed tomography, acoustic emission and ultrasonic techniques

Yidong Cai [a], Dameng Liu [a,*], Jonathan P. Mathews [b], Zhejun Pan [c], Derek Elsworth [b], Yanbin Yao [a], Junqian Li [a], Xiaoqian Guo [a]

[a] Coal Reservoir Laboratory of National Engineering Research Center of CBM Development & Utilization, School of Energy Resources, China University of Geosciences, Beijing 100083, China
[b] Department of Energy and Mineral Engineering, The EMS Energy Institute, G3 Center, Pennsylvania State University, University Park, PA 16802, USA
[c] CSIRO Earth Science and Resource Engineering, Private Bag 10, Clayton South, Victoria 3169, Australia

ARTICLE INFO

ABSTRACT

Cyclic loading of coals impacts permeability due to reversible deformation and irreversible damage and extension to pre-existing fracture networks. These changes in permeability influence the effectiveness of degassing of coal prior to mining, the recovery of coalbed methane by both conventional and enhanced methods and potential for sequestration of CO_2. We explore these interactions of stress and damage that contribute to changes in permeability through imaging with X-ray computed tomography (X-ray CT), acoustic emission (AE) profiling together with the concurrent measurement of P-wave velocities. We use these techniques to examine the evolution of the 3D fracture network during stressing through failure. A total of five semi-anthracite/anthracite coal cores (~40 mm in diameter and 80 mm in length) are sequentially loaded to failure (~37.53 MPa) with concurrent measurements of permeability. Intermittent scanning by X-ray CT, AE profiling and measurement of the evolving P-wave velocity effectively determine changes in the 3D fracture network with applied stress. These results are correlated with the "V-shaped" variation of permeability with increasing axial stress under the imposed triaxial stress conditions. This is consistent with observations on hard rocks where increasing stresses initially close fractures before fractures ultimately dilate, propagate and coalesce as the peak strength is reached. The increase in fracture volume is non uniform within the sample and is largest at the end platens. The permeability evolution was similarly dynamic with coal permeability reduced by one to two orders of magnitude in some cores (0.18–0.004 mD) until increasing dramatically as failure is approached (14.07–37.53 MPa).

© 2013 Elsevier B.V. All rights reserved.

1. Introduction

Potential unconventional natural gas resources, including coalbed methane (CBM) and shale gas, are estimated to be of the same order as the known conventional gas reserves (Karacan and Okandan, 2000). There are multiple locations where the recovery of CBM can be economically viable. However its accumulation, retention and recovery involve significantly different mechanisms to those involved in the concentration of conventional gas reserves (Ertekin, 1995; Karacan and Okandan, 2000; Vinokurova, 1978). Most significant among these is the role of matrix storage as the principal reservoir for the gas — both in free state and sorbed. Generally, in bituminous coals, CBM is produced by diffusion from the matrix micropore system to the cleats and then by Darcy flow from the fracture system to the wellbore. From the viewpoint of gas production, the most important structural features of the coal are the features of the permeable fracture network (including cleats), including mineral occurrences, fracture morphology, fracture density and relating to macroscale fracture permeability (Nick et al., 1995). For CBM extraction, knowledge of the properties of the cleats is necessary as they influence the local and regional fluid flows (Close, 1993; Laubach et al., 1998). The dynamic cleat behavior influences the permeability as fractures are the major fluid pathways. Identifying the characteristics of these fractures, including their permeability anisotropy and magnitude, and their evolution with gas pressure and effective stress, are key unknowns in the recovery of CBM. Field and laboratory studies have shown that fluid flow through natural fractures in coal and rock differs significantly from their idealization as smooth parallel plates — due principally to the heterogeneous distribution of apertures (Cacas et al., 1990; Nemoto et al., 2009; Watanabe et al., 2008, 2011a,b).

Previous research (Kendall and Briggs, 1933; Stach et al., 1982) found variations in fracture intensity depending on maceral and mineral matter contents. Fracture density depends on coal rank (Law, 1993; Pattison et al., 1996) and exhibits a reverse U-shaped relationship with rank — progressing from lignites (low fracture densities) through bituminous coals (high fracture densities) to anthracite (lower fracture densities). Fracture characteristics (e.g. density, connectivity and geometry) may be acquired by image analysis of cores from CBM reservoirs

---

Table 1
Coal composition and proximate analysis of the coals tested.

Coals	Colliery	$R_{o,m}$ (%)	Proximate analysis (ad. %)				Coal composition (%)			Micro-fractures analysis	
			C	H	A	Moisture	V	I	M	D (per 9 cm^2)	Connectivity
A (CC3#-2)	Changcun, Changzhi	1.94	82.12	3.16	0.73	8.98	89.2	9.6	1.2	9	Good
B (SJZ9#-1)	Shenjiazhuang, Gaoping	2.24	79.62	3.32	1.04	10.84	86.7	10.9	2.4	75	Very good
C (WTP15#-2)	Wangtaipu, Jincheng	3.28	79.85	2.32	2.47	11.34	89.5	6.2	4.3	8	Good
D (YC4#-1)	Yangcheng, Yicheng	2.68	82.24	3.1	1.65	10.52	18.5	81.4	0.1	14	Not good
E (ZLS3#-1)	Zhulinshan, Yangcheng	2.20	82.78	3.08	1.16	9.06	69.8	28.9	1.3	15	Not good

Note: $R_{o,m}$, Maximum vitrinite reflectance; C, Carbon; H, Hydrogen; A, Ash; V, Vitrinite; I, Inertinite; M, Minerals; D, Density.

and outcrops (Wolf et al., 2004). Techniques at the sub-meter scale were employed to measure cleat densities, or cleat spacing distribution, by using X-ray CT and image analysis (Mazumder et al., 2006; Wolf et al., 2008). X-ray CT is an effective nondestructive method for analyzing internal structures in rock materials, such as fractures in coals (Cnudde and Boone, 2013; Karacan, 2009; Karpyn et al., 2009; Ketcham and Carlson, 2001; Kumar et al., 2011; Polak et al., 2003; Zhu et al., 2007). Previous studies have demonstrated the ability to determine fracture aperture distributions using X-ray CT. (Bertels et al., 2001; Johns et al., 1993; Karpyn et al., 2009; Keller, 1998; Kumar et al., 2011; Montemagno and Pyrak-Nolte, 1999; Watanabe et al., 2011a).

To better understand the factors contributing to the dynamic evolution of permeability in coal subject to variable stresses, where fracture deformation and extension may be important, monitoring and imaging via acoustic emission (AE) may provide important constraint (Backers et al., 2005; Butt, 1999; Chang and Lee, 2004; Fu, 2005; Ganne et al., 2007; He et al., 2010). However, flows in naturally fractured coal cores, which often contain distributed fractures of different apertures and at multiple length-scales, are usually difficult to evaluate. Although fracture flow analyses by numerical fracture models with heterogeneous aperture distributions may be effective (Nemoto et al., 2009; Watanabe et al., 2011b), the determination of the evolution of the fracture aperture remains an important challenge. Thus for the effective development of CBM reservoirs an understanding of fracture characteristics, including an evaluation of fracture evolution with effective stress is important. The characterization of fracture-size patterns, network geometries, and the response of fracture systems to changing effective stress conditions is an area of principal need (Laubach et al., 1998). In addition, there are limited data on cleat apertures, widths, lengths, and connectivity. In this work, five cores from the most active CBM play in China (Qinshui Basin, North China) were investigated to evaluate the effects of the evolution of fracture heterogeneity (including cleat morphology, cleat density, and cleat aperture) under variable mechanical stresses (0–37.53 MPa) on permeability. X-ray CT, AE, P-wave velocities, and optical microscopy were combined for fracture analysis and to determine the influence of fracture network evolution on permeability as tri-axial stresses (axial differential stress in the range of 0–37.53 MPa) were incremented on naturally fractured coals.

2. Methods

2.1. Sampling and acoustic measurements

Five fresh block samples of coal (Table 1) of dimension ~30 × 30 × 30 cm^3 each were obtained directly from underground mines at depths between ~400 m and ~1200 m in the Qinshui Basin, North China using the channel method.

AE is a useful method to determine the interior dynamic change (Deng et al., 2011; Wu et al., 2011; Zhao and Jiang, 2010) of rocks. Here the AE monitoring of fracture evolution was performed using an advanced AE21C system using a single sensor with a resonant frequency of 140 kHz. The sensor was glued to the cores and further secured with spring clips or adhesive tape (Fig. 1). The AE signals were amplified by a 40 dB fixed-gain preamplifier with 110 V adaptive voltage. The detection interval was 300 μs. The AE data included: ring-down count rates, energy rates, duration and rise time (Chang and Lee, 2004) under axial compression during the cyclic loading process. Only the ring-down count rates and energy rates were used in the present study as they directly relate to fracture generation (Zhao and Jiang, 2010). P-wave velocity of coal cores was captured using a ULT-100
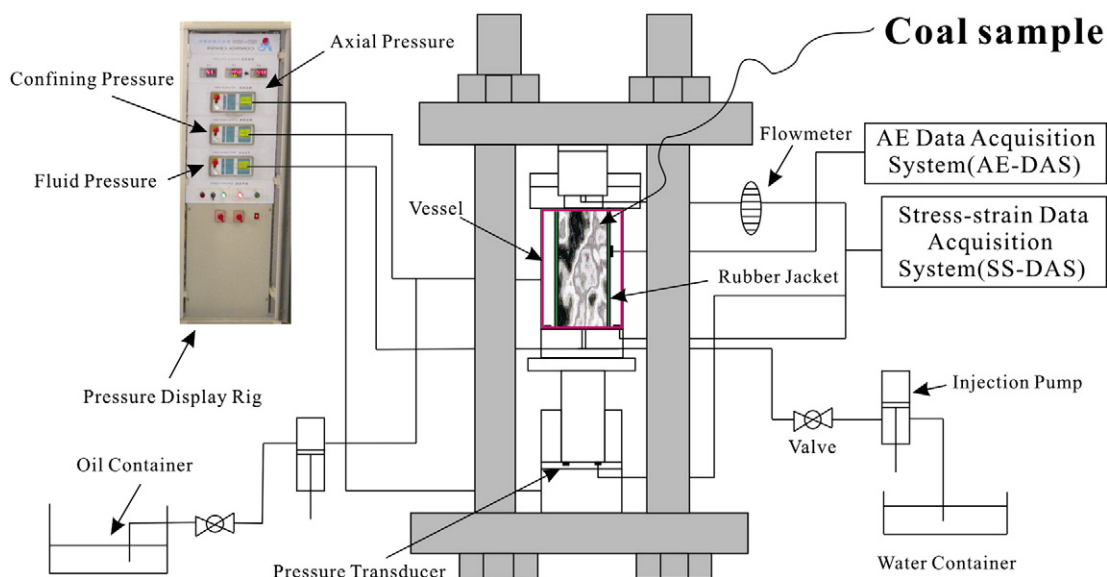
Fig. 1. Schematic plot of experimental apparatus (GAW-2000).

Table 2
Sample information and mechanical properties of the coals.

Coals	D (mm)	L (mm)	W_n (g)	Density (g/cm³)	Uniaxial mechanical properties			Vp (10^3 m/s)
					E(MPa)	υ	Co(MPa)	
A (CC3#-2)	38.00	77.50	121.12	1.38	2200	0.3	14.2	1.71
B (SJZ9#-1)	38.14	80.85	132.36	1.44	3690	0.21	20.3	2.13
C (WTP15#-2)	39.04	81.48	163.80	1.68	2270	0.37	13.2	1.89
D (YC4#-1)	38.33	82.08	139.38	1.47	4830	0.28	22.4	2.41
E (ZLS3#-1)	38.49	82.02	133.77	1.40	3610	0.32	26.1	2.09

Note: D, Diameter; L, Length; W_n, Natural weight; Vp, P wave velocity of natural coal core without stress applied; E, Young's modulus; υ, Poisson ratio; Co, Pressive strength.

system manufactured by GCTS, USA before and after the cyclic loading. The pulsing and receiving mechanisms of the ULT-100 system were used with an anti-alias filter and were digitally controlled. This system acquires data at a rate of 20 MHz with a 12 bit digitizing board and a 10 MHz bandwidth receiver.

2.2. X-ray computed tomography

The X-ray CT scans were performed as documented previously (Cai et al., 2013; Yao et al., 2009, 2010) on coal cores both before and following the application of mechanical stress. The optimal scanning settings that produced the least pixel noise and image artifacts but the highest signal-to-noise ratio for the images were at a source voltage of 180 kV and source current of 400 µA (Ketcham and Carlson, 2001). CT measurements are subjected to a variety of errors and image artifacts (Cnudde and Boone, 2013; Cnudde et al., 2006; Karacan and Okandan, 2001; Ketcham and Carlson, 2001; Mathews et al., 2011; Montemagno and Pyrak-Nolte, 1999; Yao et al., 2009). Beam-hardening is the most common, which leads to spuriously high CT numbers (Akin and Kovscek, 2003) and is manifest as a homogeneous object appearing denser around its periphery/circumference (Vinegar and Wellington, 1987; Guo, 2008). This artifact can be reduced by either core holder or CT calibration. For our experiments the CT instrument was calibrated every two samples to produce consistent images. All CT scans were performed using 100% water saturated samples at room temperature and at atmospheric pressure. Consistent scanning parameters were used for all the CT experiments to produce comparable CT images. Cores were scanned inside the core holder but without the application of confining stress before and after each cyclic loading to acquire the fracture information.

2.3. Fracture evolution under tri-axial stress and evolution of permeability

The mechanical properties and size of the coal cores are summarized in Table 2. The equipment for the measurement of fracture evolution consists of a tri-axial cell (produced by the company SUNRISE, China) with confining pressure (P_c) applied to a peak value of 70 MPa. The axial load (P_A) is applied by a mechanical press with a maximum force of 2000 kN with tests conducted under force control (Fig. 2). The overburden stress applied in the experiment σ_A on the coal can be
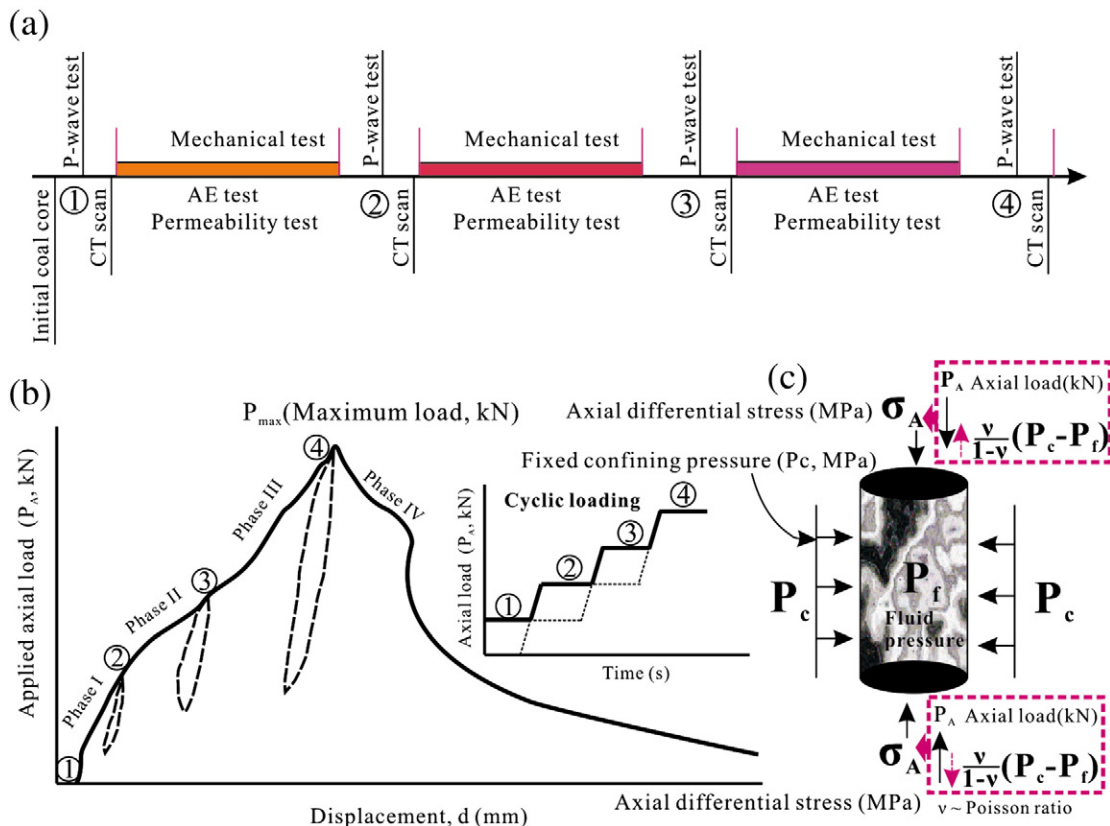

Fig. 2. (a) Flowchart of experiments, (b) fracture test of loading history for specimens (①,②,③ and ④ are four cyclic loading phases) and (c) stress state for coal cores.

Table 3
Permeability and acoustic velocity of P-wave for the coal cores and CT slice fracture area under variable axial stress.

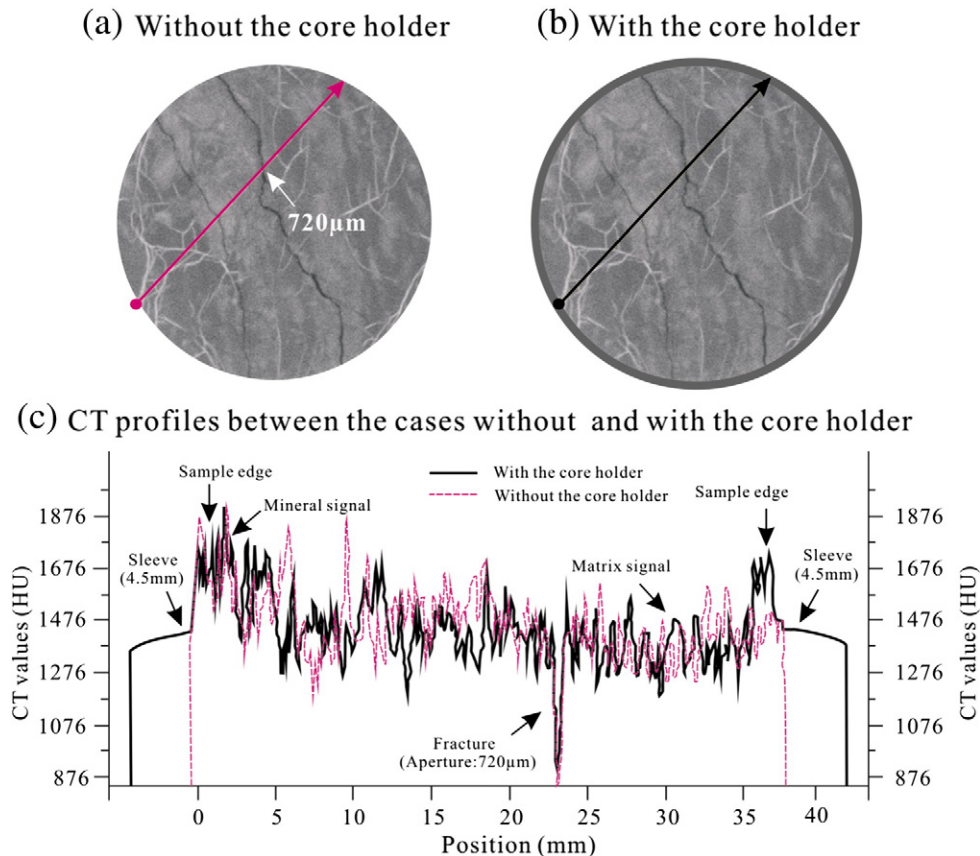| Coals	Circular no.	P_C (MPa)	P_U (MPa)	δ_A (MPa)	$V_a(10^3$ m/s)*	CT slice fracture area (mm^2)			Permeability (mD)
						Minimum	Average	Maximum	
A (CC3#-2)	A0	2; 4	1.9; 3.9	0.00	1.78	0	0.18	1.44	0.36; 0.07
	A1	2	1.9	4.37	1.24	0.01	1.31	3.08	0.072
	A2	2	1.9	7.89	1.17	0	0.51	3.1	0.324
	A3	2	1.9	14.07[f]	0.79	0.73	8.02	34.61	1.54
B (SJZ9#-1)	B0	2; 4; 6	1.9; 3.9; 5.9	0.00	1.96	0	0	0.02	0.033; 0.006; 0.0013
	B1	2	1.9	8.73	1.27	0.04	0.12	0.2	0.00359
	B2	2	1.9	14.42	1.24	0	0.11	2.65	0.015
	B3	2	1.9	26.23[f]	0.96	0.04	0.71	2.12	0.075
C (WTP15#-2)	C0	2; 4	1.9; 3.9	0.00	1.98	0	0.08	1.86	0.179; 0.035
	C1	2	1.9	8.30	1.27	3.22	21.41	112.67	0.072
	C2	2	1.9	16.65	0.97	3.01	10.42	50.84	0.036
	C3	2	1.9	37.53[f]	0.48	5.04	110.97	727.17	0.143
D (YC4#-1)	D0	2; 4; 6	1.9; 3.9; 5.9	0.00	2.53	0.1	0.96	11.94	0.038; 0.0016; 0.0004
	D1	2	1.9	10.37	1.41	4.24	6.24	28.7	0.0046
	D2	2	1.9	19.04	1.36	2.05	3.63	33.23	0.038
	D3	2	1.9	30.31[f]	0.93	2.6	28.07	83.96	0.076
E (ZLS3#-1)	E0	2; 4	1.9; 3.9	0.00	2.44	0.65	6.52	80.83	0.11; 0.018
	E1	2	1.9	5.97	1.34	5.15	10.45	70.89	0.036
	E2	2	1.9	10.26	1.28	13.78	45.63	539.1	0.33
	E3	2	1.9	16.27[f]	0.94	1.37	19.43	181.77	0.88

Note: P_C, Confining pressure; P_U, Upstream pressure; δ_A, Axial stress; V_a*, P-wave velocity of water saturated coal without stress applied; 14.07[f], failure stress.

acquired from applied axial load P_A and confining stress P_c. The applied axial load P_A is partly counteracted by the confining stress P_c, thus the axial differential stress σ_A is:

$$\sigma_A = \frac{P_A}{\pi r^2} \times 10 - \frac{v}{1-v}(P_c - P_f) \tag{1}$$

where r is the radius of coal core (cm); v is the stationary Poisson's ratio; P_f is fluid pressure in pores and fractures.

The macroscopic deformation and failure of coal occur in four phases (Medhurst and Brown, 1998), (Fig. 2): phase I, the compaction phase (from ① to ②); phase II, the apparent linear elastic deformation phase (from ② to ③); phase III, the accelerated non-elastic deformation phase (from ③ to ④); and phase IV, the rupture and development phase (after ④). These permeability experiments under cyclic loading and within the pressure vessel allowed the determination of permeability during the full stress–strain cycle (Table 3). Water

(a) Without the core holder

(b) With the core holder

720μm

(c) CT profiles between the cases without and with the core holder

Fig. 3. Signals observed in the X-ray CT scanning for the fracture aperture calibration standards (a) without and (b) with the core holder, where the fracture aperture is 720 μm and (c) CT profiles between the cases without and with the core holder.

permeability of the samples was measured under steady conditions using Darcy's law, as:

$$k = -\frac{q}{A}\frac{\mu}{\rho g}\left(\frac{\partial p}{\partial s}\right)^{-1} \qquad (2)$$

where q is the liquid (water) volume recovered in unit time for axial flow along a sample of length, ds and cross-sectional area (A); μ is the fluid viscosity; ρ is fluid density; g is gravity; $\partial p/\partial s$ is the hydraulic gradient in the direction of S.

3. Data processing

3.1. 3D reconstruction of X-ray CT slices

Five coal cores (cored parallel to the bedding plane) of approximately 8 cm length and 4 cm diameter were cut from each block to analyze the permeability changes under applied tri-axial stresses. The evolution of fractures under the application of various hydrostatic stresses was obtained indirectly via measurements of permeability and directly through acoustic emission monitoring. All cores were also scanned by X-ray CT to directly evaluate transformations in the fracture network. The CT slice thicknesses (0.15 mm) and slice increments (0.9 mm) were retained as small as feasible to enhance both resolution and contrast. For ease of data management and to reduce scanning expense slices were taken at periodic intervals (0.9 mm) rather than scanning the whole volume. A method of progressive averaging was employed to produce core visualizations using the Mimics™ software. The scanner produces images of 1024 × 1024 pixels with a pixel resolution of $40 \times 40\ \mu m^2$. The basic principle of the μCT technique is the same as

that for the conventional CT, with details provided elsewhere (Cnudde and Boone, 2013; Cnudde et al., 2006; Flannery et al., 1987; Ketcham and Carlson, 2001; Mathews et al., 2011; Montemagno and Pyrak-Nolte, 1999; Yao et al., 2009). It is usually impractical to deal with the X-ray attenuation coefficients thus, CT numbers were solely employed (Karacan and Okandan, 2001) in the reduction of data where:

$$CT_{number} = \left(\frac{\mu_c - \mu_w}{\mu_w}\right) \times 1000. \qquad (3)$$

In this relationship, μ_c is the calculated X-ray attenuation coefficient and μ_w is the attenuation coefficient for water (Hunt et al., 1987; Karacan and Okandan, 2001). X-ray CT scanning to calibrate for fracture aperture was completed both without and with the core holder (Fig. 3). Detailed discussion on the calibrations and X-ray artifacts are reported elsewhere (Ketcham and Carlson, 2001; Remeysen and Swennen, 2006; Yao et al., 2010). Fracture voids, minerals and coal matrix can be distinguished by CT values due to the density difference. Generally, the CT value of minerals is >1600 HU; the CT value of fractures is commonly <600 HU; and the CT value of the coal matrix is intermediate to this range from 600 to 1600 HU. However, detailed thresholds vary from sample to sample and relate to the calibration. Each CT scan produces a series of CT images (~80 slices for each scan). In total, 1741 images were produced from the five coal cores at 4 different conditions of hydrostatic stress. These images were analyzed using standard image analysis techniques (Mimics 10™ and PS 6.0™) to quantify the fracture area within each slice. Slices of each CT scan were also stacked in Mimics™ to produce virtual core sections (multi-planar reconstruction) throughout the volume data set to show the inner heterogeneity within the cores. Fracture area was also quantified
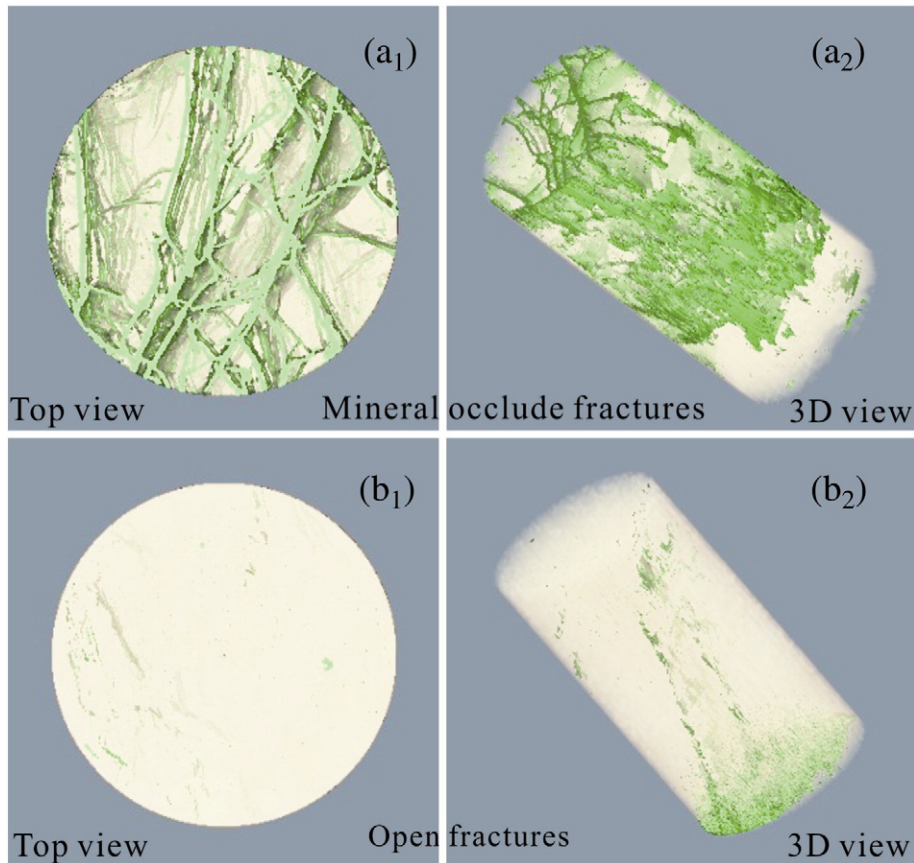

Fig. 4. 3D performance of mineral occluded fractures (view top to bottom for a_1 and a_2) and open fractures (b_1 and b_2) in the initial core A by Mimics™ (3D view from top to bottom for a_1 and b_1; lateral 3D view for a_2 and b_2).

using Fovea Pro and Photoshop in an automated image processing and image analysis approach (Kumar et al., 2011).

3.2. Fracture and fracture flow

To develop 3D models of coal cores, it is necessary to covert CT images into the 3D fracture aperture distributions (Bertels et al., 2001; Johns et al., 1993; Keller, 1998; Watanabe et al., 2011a). Since CT values increase with density (and atomic number), they are used to distinguish between mineral-filled and open fractures Fig. 4. Fracture apertures can be determined as shown in Fig. 3. Due to the limitation of voxel size of the CT images only apertures of >40 μm can be resolved. For single phase fluid flow the relationship between the square of the permeability and the fracture aperture has been proposed (Elsworth and Goodman, 1986; McKee and Bumb, 1988), namely:

$$k_l = \frac{w_f^2}{12} \cdot \phi_f \qquad (4)$$

where, k_l is the local permeability (mD); ϕ_f is fracture porosity (decimal); w_f is fracture aperture (mm). Thus, the larger fracture apertures have much higher permeabilities. Fracture porosity is determined through a Boolean calculation as described previously (Yao et al., 2009). Here a segmentation method was used to acquire the area of fractures in each CT slice using PS 6.0™. Consequently, the porosity of the core is calculated by averaging the slice fracture porosity of all slices. Furthermore, the local fracture permeability is evaluated from the CT data. For a single fracture, the fracture permeability is constrained by the narrowest section.

4. Results and discussions

4.1. Coal analysis

All coal samples were carefully packed at the mine face and were quickly transported to the laboratory for immediate use. The proximate analysis, vitrinite reflectance, and fracture observation (by eye) are shown in Table 1. Vitrinite reflectance ($R_{o,m}$), coal composition and micro-fracture analyses were carried out on polished slabs of about 30×30 mm^2 squared. These analyses were performed on the Laborlxe 12 POL microscope with the MPS 60 photo system manufactured by Leitz Company of Germany (Cai et al., 2011; Liu et al., 2009). Samples had vitrinite reflectance ($R_{o,m}$) values in the range of 1.8%–3.28%, thus were semi-anthracite to anthracite. Micro-fracture density has strong microscopic heterogeneity for sample B (75 per 9 cm^2).

4.2. 3D visualization of fractures by X-ray CT

The 3D reconstruction of coal cores generated from the X-ray CT consists of gray scale pixels. Typical results for natural fractures of coal core samples are shown in Figs. 3 and 4. Minerals have a higher density and atomic number than the coal and show as bright white particles or bands in a gray value. There are obvious differences between open and mineral occluded fractures. The natural fracture network of the coals appears as green lines, mostly linear but with some laminar fractures as shown in Fig. 4, which has a heterogeneous distribution but with good connectivity. The non-mineral occluded fractures are less developed (normally short with poorer connectivity), which is likely related to stress intensity at post diagenesis and hydrodynamic conditions. Theoretically, the local distribution of the open micro-fractures depends
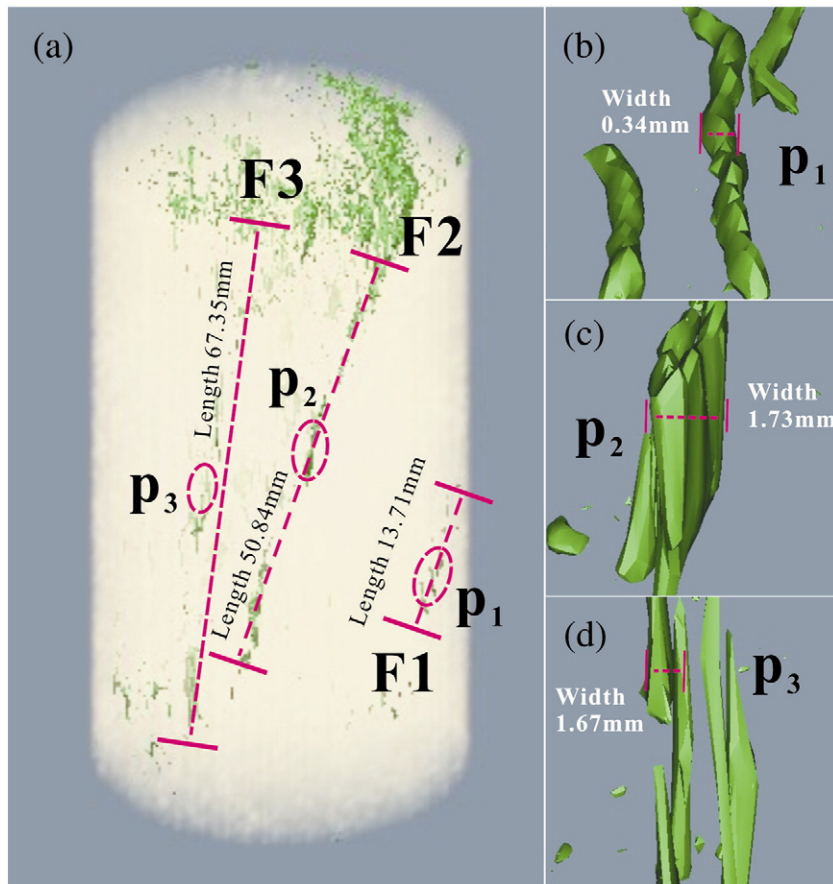

Fig. 5. 3D reconstructions of fractures and quantitative length and width of apertures for core A at the last cyclic stage (F1, F2 and F3 are the main fractures generated; p₁ for F1; p₂ for F2; p₃ for F3).

on the boundaries between the coal matrix and minerals. Cleats are more easily identifiable when minerals are present (Golab et al., 2013). To aid in viewing the cleat structure of the coal core A at the fourth cyclical loading stage, the fractures have been made more visible by false coloring and a 3D view consisting of three fractures (F1, F2 and F3) is shown in Fig. 5. The length of these three fractures were determined to be 13.71 mm, 50.84 mm and 67.35 mm for fractures F1, F2 and F3 respectively. The fine details of fracture apertures were observed and measured by using Mimics™ software (Yao et al., 2009). Fractures appear mostly in thin bands within the core indicating more small fractures created during axial compression under tri-axial condition. At axial stress conditions the long fracture (fracture F3) are presumably aligned parallel to the unique compressional axis (δ_A). The fracture F3 is the main fracture in core A. In this coal core, the minerals do not fully occlude the fractures and therefore cleats function as fluid flow pathways. Three sets of fractures are visible in Fig. 5. For fracture F1, the largest width is 0.83 mm and it is short, which could not be the main fracture in core A. Although, the fracture F2 has the widest fracture that is close to 5 mm, it has the weak connectivity of inner fracture. However, it is slightly connected to the longest fracture F3, and thus is the main contribution to permeability.

4.3. Fracture evolution under cyclic loading

The CT scanner produces a series of gray images with 1024×1024 pixels for a slice. In the gray image, each pixel has a gray value between 0 and 255. The fracture has certain gray value intervals. The segmentation technique first defines an upper and a lower threshold of CT numbers for the fracture. Then the area with the CT numbers between the lower and upper thresholds is defined as the region of the fractures. After that the averaged CT numbers were acquired from the lower and upper thresholds, which were defined to be T_G. A Boolean calculation for the gray image was conducted by defining a threshold T_G, which divided each pixel into the binary value of 0 and 1:

$$f(x,y) = \begin{cases} 0 & p(x,y) \leq T_G \\ 1 & p(x,y) > T_G \end{cases} \tag{4}$$

where, $p(x,y)$ is the raw gray value of a pixel at location of (x,y), $f(x,y)$ is the value after binary process. Based on the Boolean calculation, the CT image is transformed into a black–white image, in which the black area $(f = 0)$ is for fractures and the white area is for coal matrix $(f = 1)$ (Yao et al., 2009). As a result, the slice fracture area can be acquired. This method was applied to obtain the fracture area of all slices at different cyclical loading stage. The dynamic change in the fracture area for each slice location at different cyclic loadings is shown in Fig. 6, which increased one to two orders of magnitudes from linear compression to core failure stage (phase I to phase IV) for almost every coal core. The axial stress of core A increased from 0 MPa to 14.4 MPa during the cyclic loading history, which caused the fracture area increased from 1.41 mm² to 33.01 mm². Although there was a slight deviation of fracture position, the memory effect is apparent between A0 to A3 (Fig. 6). Apparently, all cores have this memory effect (fracture extension follows the original fracture track) of fracture during reloading of the axial stress, which is similar as the Kaiser effect for acoustic emission of fracture during axial reloading (Deng et al., 2011). Another interesting phenomenon is a large increase of fracture area between cyclic A2 and A3, which reveals that the accelerated non-elastic deformation phase was the most important stage for fracture creation. For the other coal cores there were similar observations. Core C has the highest axial stress (37.53 MPa) for failure and has the largest fracture area at the last cyclic stage. This is expected to relate to the coalification process. Core C has the highest $R_{o,m}$ 3.28%. For these samples coals with a higher $R_{o,m}$ had the higher axial failure stress as shown in Fig. 6.
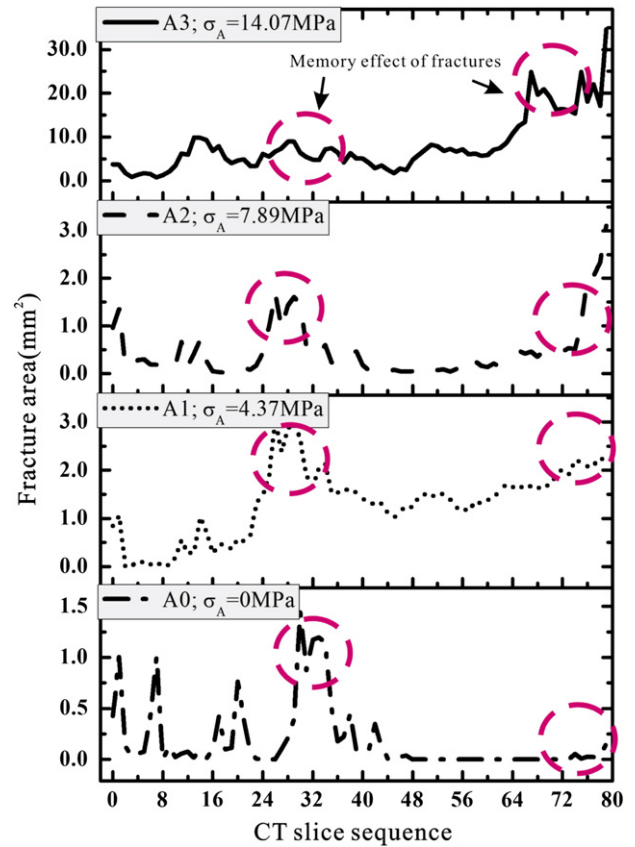

Fig. 6. Memory effect of fracture extension for core A under cyclic axial loading.

4.4. Acoustic characteristics for fracture evolution

4.4.1. Acoustic emission at the last cyclic stage

AE techniques have been used to quantify how coal and rocks fail (Cox and Meredith, 1993; He et al., 2010; Zhao and Jiang, 2010). Generally, at low stress, AE events are broadly distributed throughout the core, indicating that the deformation is quasi-homogeneously distributed The AE energy and count-down rates increased suddenly at 0.23 σ_m (σ_m is the compressive strength) and 0.82 σ_m under uniaxial condition (Zhao and Jiang, 2010), which shows 0.23 σ_m and 0.82 σ_m are the main starting points for the micro-fracture generation. To analyze the effect of original micro-fractures in coals on AE events, a micro-fractures analysis was conducted. The original cores differ in micro-fracture density from visual observation, ranging from 8 per 9 cm² (sample C) to 75 per 9 cm² (sample B) (Table 1). The micro-fractures affect the mechanical properties (Young's modulus, Poisson ratio, coal strength, etc.). The obvious positive relation exists between the coal strength and micro-fracture density (Tables 1 and 2). The macroscopic deformation and failure of coals can be divided into four phases as documented in Section 2.4 (Medhurst and Brown, 1998; Song et al., 2012). In the early cyclic loading process, with relatively intact internal structure, coal mass has strong capacity of elastic recovery and resisting external load. Most energy input this period can be preserved in the form of elastic energy, which can be refreshed when the load decreases, leading to a small hysteresis loop in this phase; in the later cyclic loading phase, the internal structure of the samples are destroyed, reducing the capacity for external load bearing and storing elastic energy. The deformation of cores by external load is released mostly as dissipated energy, which leads to weak elastic recovery when external load decreases, creating the hysteresis loop as shown in Fig. 2. In the compaction phase (before point II), almost all original defects in coal mass are deformed. New micro-fractures, are formed (AE signal intensity) and increase at the beginning

of the applied mechanical stress then decrease. In the selected coal cores (core A, core B and core C for AE consideration), only core B has this performance, which shows very low ring-down count rates and energy rates as shown in Fig. 7. The permeability is in the range of 1.54 mD, 0.075 mD and 0.143 mD for core A, core B and core C, respectively. The lowest permeability is core B. In the apparent linear elastic deformation phase (from points II to III), the generation of AE signals in microenvironment was episodic rather than continuous. Only the deformation energy in coal can accumulate high enough to cause medium fractures and generate strong AE signals. The ring-down count rates are generally high, while energy rates are low. This reveals that there are many micro- and medium-fractures generated but few macro-fractures. It is especially obvious for core A and core B (Fig. 7). In contrast, the macro-fracture signals increase continuously in a nearly linear mode. This is a relatively stable phase. With increasing deviatoric stresses and the generation of new fractures, AE counts and energy gradually increases prior to the failure of the sample when event rates increase drastically (Wang et al., 2013). In the accelerated non-elastic deformation phases (III to IV in Fig. 7), large amounts of elastic–plastic energies are accumulated in coal mass, resulting in sharply increased AE counts. Although a few macro-fractures were generated in this phase, they normally have the almost strongest AE signals including ring-down count rates and energy rates. The total AE count rates for core A (1.94% $R_{o,m}$), B (2.24% $R_{o,m}$) and C (3.28% $R_{o,m}$) were 0.76×10^4, 9.6×10^4, 72.2×10^4 respectively. This demonstrates a positive relationship between AE signals and $R_{o,m}$ (Fig. 7). The initial rapid increase of permeability under axial stress is thus primarily due to the formation of an interconnecting fracture network. After that, the increased permeability was due to an increase in the pre-existing fracture apertures and marked generation of new fractures (Figs. 6 and 7).

4.4.2. P-wave velocity of coal cores

For the travel paths of the P-wave, which is parallel to the sample axis, the P-wave direction/angle and velocity during deformation are strongly depending on the stress and fracture geometry. Consequently, the observed velocity signatures can be related to characteristic fracture patterns (Popp and Kern, 2000). Fracture planes are often described as penny shaped fracture, are predominantly oriented parallel to the direction of compressional axial direction (Fig. 8). P-wave velocity of the water saturated coal cores at the fourth loading stage is in the range of 0.48–0.96 km/s (Table 3; Fig. 8). These are generally lower than previous work (Zhao and Hao, 2006; Zhou, 2012), which show P-wave velocity in the range of 2.4–1.7 km/s, 2.1–1.6 km/s and 2.1–1.5 km/s for 0°, 45° and 90° respectively. The difference for P-wave velocity results are due to water saturated natural coals in this work and dry coals with artificial fractures in the previous research. Despite these differences they have the same trend between P-wave velocity and angles. The result shows that P-wave velocity has a decreasing trend with increasing angle between P-wave and fracture (from 0° to 90°) as shown in Fig. 8. Many factors including: fracture anisotropy, extent and placement of occluded minerals, stresses, and water saturation affect the P-wave propagation across the coal cores, thus these factors should be isolated to evaluate its effect. Previous research (Zhao and Hao, 2006) reveals that the P-wave velocity and angles have a periodic (180° of

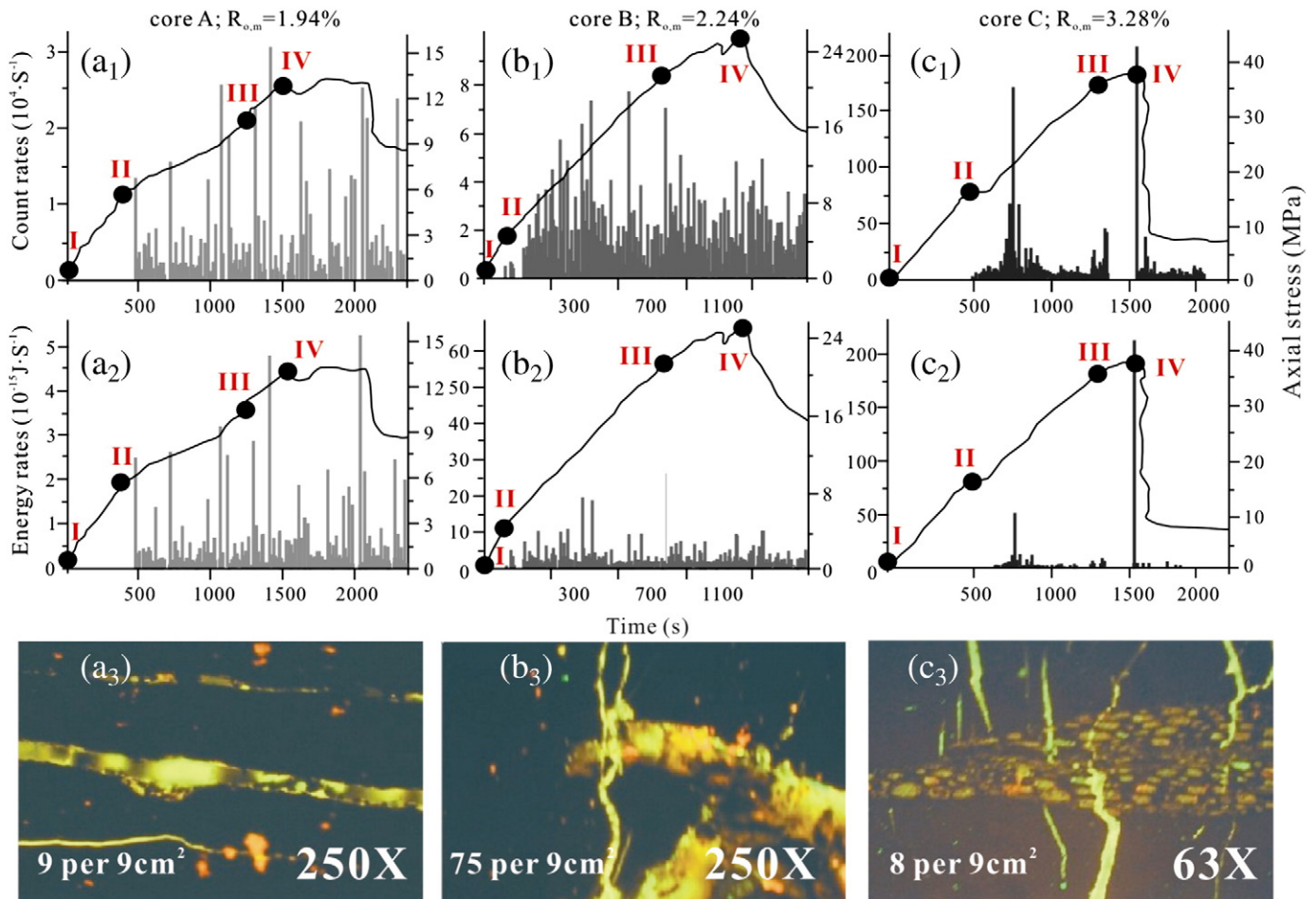**Fig. 7.** Count rates (a₁, b₁, and c₁), energy rates (a₂, b₂, and c₂) of acoustic emission and fracture density quantified by fluorescence microscopic for selected samples at the last cyclic stage (a₃, b₃, and c₃).
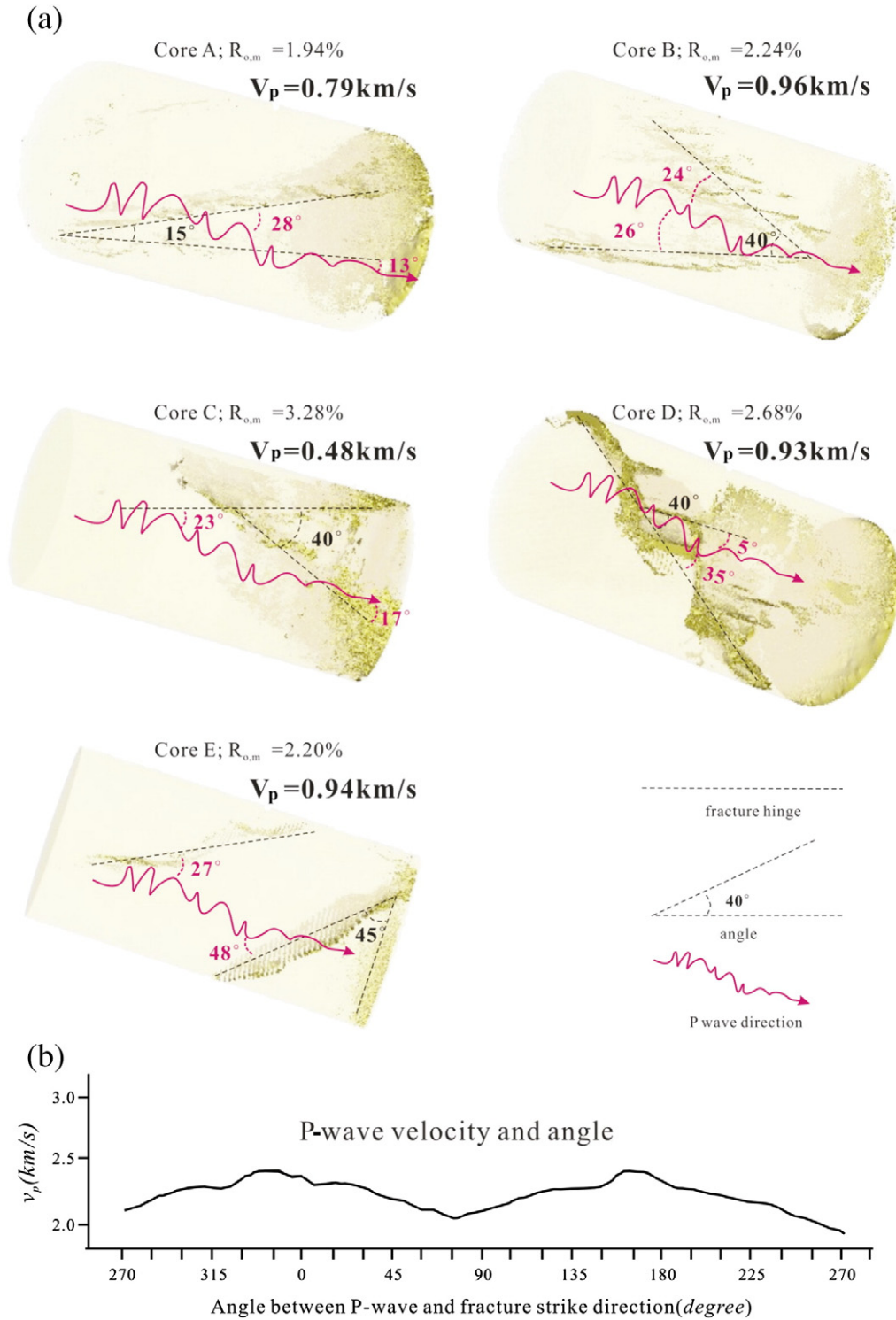
Fig. 8. 3D distributions of fractures for core specimens at the last cyclic stage (a) and relationship between P-wave velocity and angles (b) (b adapted from Zhao and Hao, 2006).

one period) relationship: the P-wave velocity goes up from close 90° to 180°, and then drops down from 180° to 270°. Although those experiments were conducted on artificially fractured coal cores, it still has the reference significance for natural coals.

As mentioned, P-wave velocity is also affected by stresses. Previous work (Meng et al., 2008; Zhou, 2012) has confirmed that P-wave velocity has a positive relationship with increasing confining pressures. However, they did not include the impact of axial stresses on P-wave velocity. What is needed is an experiment approach to observe changes of P-wave velocity accompanying increasing axial stresses. The P-wave

velocity has a negative trend with increasing axial stresses. The original water saturated coal cores normally have 1.78–2.53 km/s of P-wave velocity as shown in Fig. 9. The axial stress in the compression phase causes many of the micro fractures to be close (or reduce apertures), while the measurement of P-wave velocity was conducted without stress applied. Thus a large number of micro-fractures in cores can lower the strength of the coals. Thus the P-wave velocity has a sharp decrease. At the next phase (the apparent linear elastic deformation phase), a steady increase of micro-fractures is generated, thus a slight decrease of the P-wave velocity accompanied this phase. At the
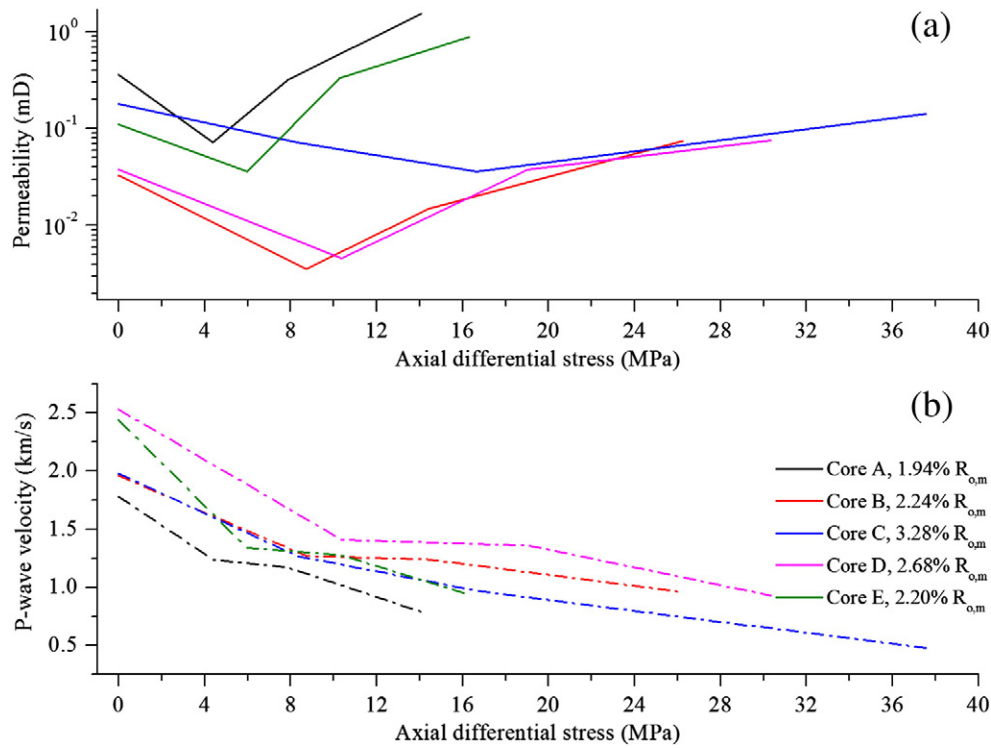
Fig. 9. Relationship between permeability, P wave velocity and increasing axial pressure for water saturated coal specimens.

accelerated non-elastic deformation phase, multiple fractures will be generated due to the extensive axial compress stress until failure (Wang et al., 2013; Zhao and Jiang, 2010), which makes the P-wave velocity decrease. P-wave normally has an average velocity of ~0.9 km/s when the cores are in the phase of coal failure phase. The core permeability has a negative relationship with P-wave velocity after the linear elastic phase, and is highly directional dependent.

4.5. Fluid flow under tri-axial stresses

4.5.1. Axial stress on coal permeability

The permeability is related to fracture evolution (Rowland et al., 2008). As revealed in Fig. 10, the fracture area increased with increasing axial stress, which was acquired without any stresses applied as observed by CT images. The average fracture area from CT slices of core A increased from 0.18 to 8.02 mm², core B from 0 to 0.71 mm², core C from 0.08 to 110.97 mm², core D from 0.96 to 28.08 mm², and core E from 6.52 to 19.43 mm². Most increased by one to two orders of magnitude. For core C, the area increased by four orders of magnitude. The permeability of coal cores different angles between main fractures and axial direction are in the order of 1.54 mD for 13°, 0.179 mD for 24°–26°, 0.038 mD for 17°–23°, 0.076 mD for 35°, and 0.88 mD for 27°–48 respectively by Eq. (2). The fractures opened in the "wrong" direction would result in the variation of permeability observed during axial stress which is remarkably low (Popp and Kern, 2000). Previous research reveals that permeability changes little with the presence of a radial fracture across the sample. However, the permeability increases by three orders of magnitude with a longitudinal fracture through the sample (Wang et al., 2011). Even though core C has the largest fracture area, it does not control the highest permeability due to the weak connectivity of the fractures within core (Fig. 8). Core A has the largest permeability after the last cyclic process, as the fracture occurs over the entire core length. The fracture connectivity is expected to be more important to permeability than the shape, distribution or length of the coal cores in those localized regions.

The permeability shows a "V-shaped" with respect to increasing axial differential stress (Fig. 10). This could be attributed to two

different mechanisms: (1) decreasing permeability due to the core compaction at early stages and (2) increasing permeability due to the complex process of facture generation, dilatancy and less compaction at late stages (Wang et al., 2013). These data were well fitted with simplified proelastic permeability (PP) model (Gray, 1987) at early stages and fracture-porosity based permeability (FPP) model (Palmer and Mansoori, 1998) as shown in Fig. 10. A simplified proelastic model between effective stress and permeability was proposed by Grays (1987)

$$\frac{k}{k_0} = \exp\left(-\frac{3\sigma_e^h}{E_f}\right) \tag{5}$$

where E_f is an analogous Young's modulus for the fracture. k_0 is initial permeability, mD. σ_e^h is the effective stress in horizontal plane. A widely applied fracture-porosity based permeability model to describe the permeability change with respect to porosity change is (e.g. Palmer and Mansoori, 1998)

$$\frac{k}{k_0} = \left(\frac{\phi}{\phi_0}\right)^3 \tag{6}$$

where ϕ is fracture porosity. ϕ_0 is initial fracture porosity. At the first cyclic loading stage, when the axial stress increases, the original fractures or some pores are compressed to be closed, thus the permeability will show a decrease at the first cyclic except the core C. The decreasing trend of permeability extending to the second cyclic loading should be related to its special compaction phase that owns strong capability to resist compaction (Yu et al., 2013). At the second cyclic loading stage, when further axial stress increases, the axial compression produced many fractures with a low to medium energy rate by longitudinal deformation, confirmed by AE signals as shown in Fig. 7, thus its permeability increased quickly. With the increasing axial stress, the fracture had an accelerated development. The main fractures were generated and connected; the main fracture flow path was created in this phase (Fig. 11), and thus the higher permeability. Based on Eq. (4), the local permeability for one of the main fractures (fracture
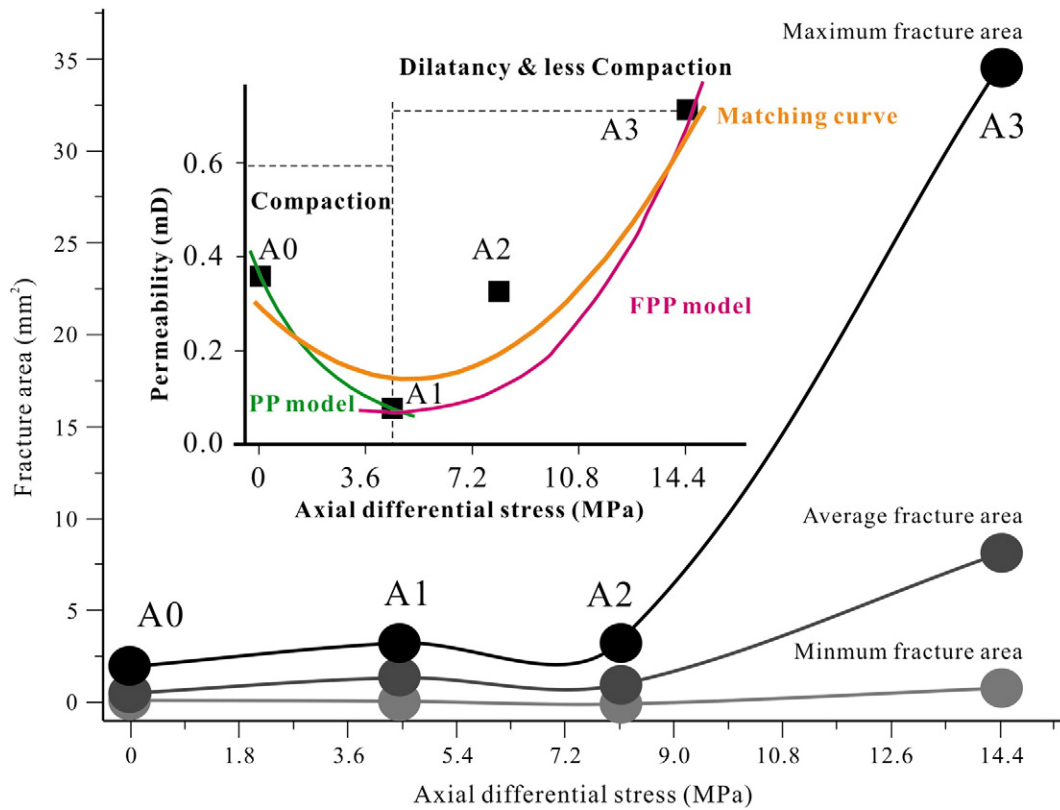
Fig. 10. Permeability variations and fracture area (minimum, average and maximum) under cyclic axial differential stresses for core A by X-ray CT.

F3) based on the fracture aperture was predicted to be in the range of 0.01–0.33 mD. This value was lower than the test permeability (1.54 mD) which may be due to the neglect of the other two fractures, simplistic modeling equation and CT scan constrains.

4.5.2. Confining pressure on coal permeability

The data obtained at 2 MPa, 4.0 MPa and 6.0 MPa confining pressures were further analyzed to explore the relationship between permeability and confining stress at a constant pore pressure condition. Confining pressure often influences coal permeability, as the confining pressure increases, core permeability decreases (Pan et al., 2010). This is because the core deformation tends to narrow down the fractured flow channel, leading to flow rate decrease, and thus permeability reduction. Since the axial water flow, with the confining pressure increases, the fracture aperture narrows, exacerbating the trend of reduced permeability (Yu et al., 2013). For all tested samples in the case of an increase of the confining pressure, there is a decrease of the permeability as shown in Fig. 12. The permeability decrease is very significant. In this study, the permeability of coal containing fractures under 2 MPa confining pressure at the initial conditions are in the order of 0.36 mD for core A, 0.033 mD for core B, 0.179 mD for core C, 0.038 mD for core D and 0.11 mD for core E, respectively. The permeability of cores under 4 MPa confining pressure are 0.07 mD for core A, 0.006 mD for core B, 0.035 mD for core C, 0.0016 mD for core D and 0.018 mD for core E respectively, which have a similar trend as the literature (Vishal et al., 2013). As the confining pressure increases, coal permeability reduces by one to two orders of magnitude.

5. Conclusions

A series of experiments were run on coal samples that included imaging by X-ray CT, AE counts, and measuring changes in P-wave velocity and permeability. These experiments were run to failure on semi-anthracite to antracite cores under tri-axial compression to determine the fracture/permeability evolution under cyclic loading (mechanical stress). The permeability change with respect to confining pressure was evaluated. The following conclusions were made:

1. Imaging by X-ray CT was coupled with measurements of AE and P-wave velocity to follow fracture evolution under cyclic loading. The principal (largest) fractures that develop during the cyclic loading process can be determined by 3D reconstruction of CT slices and AE. Fine details of fractures can be acquired to show the fracture density, orientation, and apertures and infer impacts on local permeability.

2. During the cyclic loading process, all cores exhibited a memory effect on fractures during reloading by the axial stress — which is similar to the Kaiser effect for acoustic emission but related to the fracture during axial reloading. This is verified by measurements of fracture area evolution calculated from the CT slices. Furthermore, it was shown that for these samples the higher the rank of coals ($R_{o,m}$), the higher is the axial failure stress.

3. The effects of orientation angles between fractures relative to the P-wave direction on P-wave velocity were analyzed. It shows that the P-wave velocity decreases with increasing angle between the P-wave travel direction and the fracture (from 0° to 90°). Furthermore, the P-wave velocity decreases with increasing axial stresses due to the creation of fractures within the coal.

4. Coal permeability is directly related to fracture connectivity, geometry (fracture aperture, fracture plane and angle etc.), density and stress conditions. Permeability decreases under loading as P-wave velocity increases. A model of stress-controlled fracture closure and opening in the triaxial stress regimes presents a physically realistic explanation that is consistent with the signals from AE, P-wave velocity trends and the permeability observed in the triaxial stress experiments.
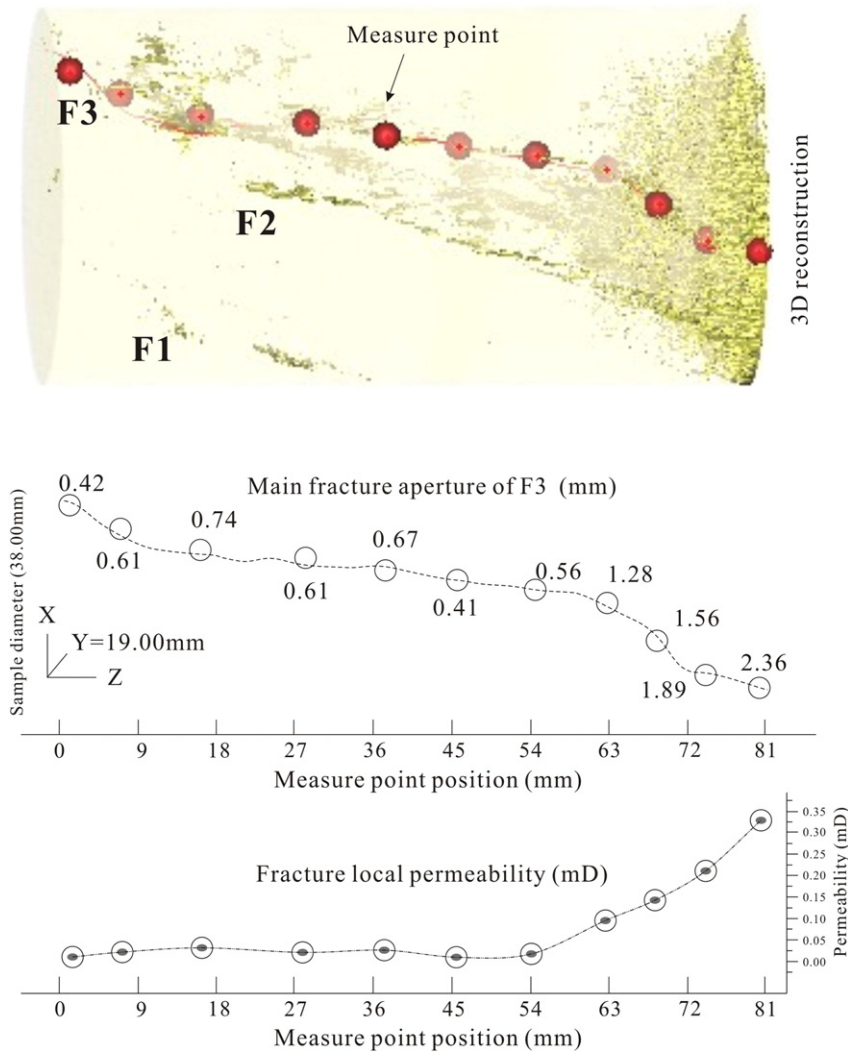
Fig. 11. Fracture aperture and local permeability for core A at the last cyclic stage (F1, F2 and F3 are the main fractures).

5. A "V-shaped" plot of permeability varies with applied stress results. This is closely related to the phases of deformation and failure of the coal mass. Furthermore, as the confining pressure increases, coal permeability reduces by one to two orders of magnitude. The amplitude of permeability reduction decreases at higher confining pressures.
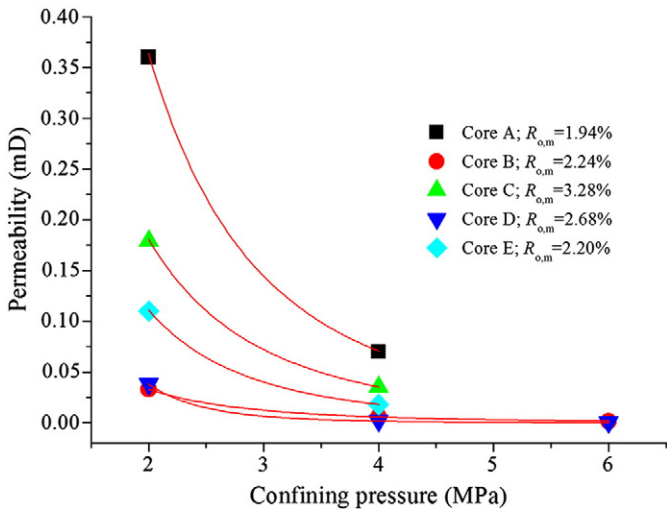
Fig. 12. Relationship between permeability and confining pressure.

References

Akin, J.C., Kovscek, A.R., 2003. Computerised tomography in petroleum engineering research. Applications of Computerized X-ray Tomography in Geology and Related Domains. In: Jacobs, P., Mees, F., Swennen, R., Van Geet, M. (Eds.), vol. 215. Geological Society, London, pp. 23–38 (Special Publication).

Backers, T., Stanchits, S., Dresen, G., 2005. Tensile fracture propagation and acoustic emission activity in sandstone: the effect of loading rate. Int. J. Rock Mech. Min. Sci. 42, 1094–1101.

Bertels, S.P., DiCarlo, D.A., Blunt, M.J., 2001. Measurement of aperture distribution, capillary pressure, relative permeability, and in-situ saturation in a rock fracture using computed tomography scanning. Water Resour. Res. 37 (3), 649–662.

Butt, S.D., 1999. Development of an apparatus to study the gas permeability and acoustic emission characteristics of an outburst-prone sandstone as a function of stress. Int. J. Rock Mech. Min. Sci. 36 (8), 1079–1085.

Cacas, M.C., Ledoux, E., de Marsily, G., Tillie, B., Barbreau, A., Durand, E., Feuga, B., Peaudecerf, P., 1990. Modeling fracture flow with a stochastic discrete fracture network: calibration and validation 1. Water Resour. Res. 26 (3), 479–489.

Cai, Y., Liu, D., Yao, Y., Li, J., Qiu, Y., 2011. Geological controls on prediction of coalbed methane of No. 3 coal seam in Southern Qinshui Basin, North China. Int. J. Coal Geol. 88 (2–3), 101–112.

Cai, Y., Liu, D., Pan, Z., Yao, Y., Li, J., Qiu, Y., 2013. Petrophysical characterization of Chinese coal cores with heat treatment by nuclear magnetic resonance. Fuel 108, 292–302.

Chang, S.H., Lee, C.I., 2004. Estimation of cracking and damage mechanisms in rock under triaxial compression by moment tensor analysis of acoustic emission. Int. J. Rock Mech. Min. Sci. 41, 1069–1086.

Close, J.C., 1993. Natural fractures in coal. In: Law, B.E., Rice, D.D. (Eds.), Hydrocarbons from Coal. AAPG Studies in Geology, pp. 119–132.

Cnudde, V., Boone, M.N., 2013. High-resolution X-ray computed tomography in geosciences: a review of the current technology and applications. Earth-Sci. Rev. http://dx.doi.org/10.1016/j.earscirev.2013.04.003.

Cnudde, V., Masschaele, B., Dierick, M., Vlassenbroeck, J., Van Hoorebeke, L., Jacobs, P., 2006. Recent progress in X-ray CT as a geosciences tool. Appl. Geochem. 21, 826–832.

Cox, S.J.D., Meredith, P.G., 1993. Microcrack formation and material softening in rock measured by monitoring acoustic emissions. Int. J. Rock Mech. Min. Sci. 30, 11–24.

Deng, X., Liu, X., Tian, S., 2011. Experimental study of original cracks features effecting on fracture of coal samples under uniaxial compression. Procedia Eng. 26, 681–688.

Elsworth, D., Goodman, R.E., 1986. Characterization of rock fissure hydraulic conductivity using idealized wall roughness profiles. Int. J. Rock Mech. Min. Sci. 23, 233–244.

Ertekin, T., 1995. Coalbed methane recovery modeling: what we know and what we need to learn. Turk. J. Oil Gas 1 (1), 7–18.

Flannery, B.P., Deckman, H.W., Roberge, W.G., D'Amico, K.L., 1987. Three-dimensional X-ray microtomography. Science 237, 1439–1444.

Fu, X.M., 2005. Experimental study on uniaxial compression deformation and acoustic emission property of typical rocks. J. Chengdu Univ. Technol. (Sci. Technol. Version) 31, 17–21.

Ganne, P., Vervoort, A., Wevers, M., 2007. Quantification of pre-peak brittle damage: correlation between acoustic emission and observed micro-fracturing. Int. J. Rock Mech. Min. Sci. 44, 720–729.

Golab, A., Ward, C.R., Permana, A., Lennox, P., Botha, P., 2013. High-resolution three-dimensional imaging of coal using microfocus X-ray computed tomography, with special reference to modes of mineral occurrence. Int. J. Coal Geol. 113, 97–108.

Gray, I., 1987. Reservoir engineering in coal seams: part 1—the physical process of gas storage and movement in coal seams. SPE Reserv. Eng. 2 (1), 28–34.

Guo, R., 2008. Coal Characterization in CBM/ECBM Processes Using X-ray CT Analysis. CSPG/CSEG/CWLS GeoConvention, Calgary, Alberta, Canada (May 12–15).

He, M., Miao, J., Feng, J., 2010. Rock burst process of limestone and its acoustic emission characteristics under true-triaxial unloading conditions. Int. J. Rock Mech. Min. Sci. 47, 286–298.

Hunt, P.K., Engler, P., Bajscrowicz, C., 1987. Computed tomography as a core analysis tool: applications and artifact reduction techniques. Proceedings of SPE Annual Technical Conference and Exhibition, Dallas. SPE Paper, 16952.

Johns, R.A., Steude, J.S., Castanier, L.M., Roberts, P.V., 1993. Nondestructive measurements of fracture aperture in crystalline rock cores using X-ray computed tomography. J. Geophys. Res. 98 (B2), 1889–1900.

Karacan, C.Ö., 2009. Reservoir rock properties of coal measure strata of the Lower Monongahela Group, Greene County (Southwestern Pennsylvania), from methane control and production perspectives. Int. J. Coal Geol. 78 (1), 47–64.

Karacan, C.Ö., Okandan, E., 2000. Fracture/cleat analysis of coals from Zonguldak Basin (northwestern Turkey) relative to the potential of coalbed methane production. Int. J. Coal Geol. 44 (2), 109–125.

Karacan, C.Ö., Okandan, E., 2001. Adsorption and gas transport in coal microstructure: investigation and evaluation by quantitative X-ray CT imaging. Fuel 80, 509–520.

Karpyn, Z.T., Alajmi, A., Radaelli, F., Halleck, P.M., Grader, A.S., 2009. X-ray CT and hydraulic evidence for a relationship between fracture conductivity and adjacent matrix porosity. Eng. Geol. 103 (3–4), 139–145.

Keller, A., 1998. High resolution, non-destructive measurement and characterization of fracture apertures. Int. J. Rock Mech. Min. Sci. 35 (8), 1037–1050.

Kendall, P.F., Briggs, H., 1933. The formation of rock joints and the cleat of coal. Proc. R. Soc. Edinb. 53, 164–187.

Ketcham, R.A., Carlson, W.D., 2001. Acquisition, optimization and interpretation of X-ray computed tomographic imagery: applications to the geosciences. Comput. Geosci. 27 (4), 381–400.

Kumar, H., Lester, E., Kingman, S., Avila, C., Jones, A., Robinson, J., Halleck, P.M., Mathews, J.P., 2011. Inducing fractures and increasing cleat apertures in bituminous coal under isostatic stress via application of microwave energy. Int. J. Coal Geol. 88 (1), 75–82.

Laubach, S.E., Marrett, R.A., Olson, J.E., Scott, A.R., 1998. Characteristics and origins of coal cleat: a review. Int. J. Coal Geol. 35, 175–207.

Law, B.E., 1993. The relation between coal rank and cleat spacing: implications for the prediction of permeability in coal. Proceedings of International Coalbed Methane Symposium II, pp. 435–442.

Liu, D., Yao, Y., Tang, D., Tang, S., Che, Y., Huang, W., 2009. Coal reservoir characteristics and coalbed methane resource assessment in Huainan and Huaibei coalfields, Southern North China. Int. J. Coal Geol. 79 (3), 97–112.

Mathews, J.P., Denis, J., Pone, N., Mitchell, G.D., Halleck, P., 2011. High-resolution X-ray computed tomography observations of the thermal drying of lump-sized subbituminous coal. Fuel Process. Technol. 92 (1), 58–64.

Mazumder, S., Wolf, K.-H.A.A., Elewaut, K., 2006. Application of X-ray computed tomography for analyzing cleat spacing and cleat aperture in coal samples. Int. J. Coal Geol. 68, 205–222.

Mckee, C.R., Bumb, A.C., 1988. A three-dimensional analytical model to aid in selecting monitoring locations in the vadose zone. Ground Water Monit. Rev. 8 (2), 124–136.

Medhurst, T.P., Brown, E.T., 1998. A study of the mechanical behaviour of coal for pillar design. Int. J. Rock Mech. Min. Sci. 35 (8), 1087–1105.

Meng, Z., Liu, C., He, X., Zhang, N., 2008. Experimental research on acoustic wave velocity of coal measures rocks and its influencing factors. J. Min. Saf. Eng. 25 (4), 389–393.

Montemagno, C.D., Pyrak-Nolte, L.J., 1999. Fracture network versus single fractures: measurement of fracture geometry with X-ray tomography. Phys. Chem. Earth Solid Earth Geod. 24 (7), 575–579.

Nemoto, K., Watanabe, N., Hirano, N., Tsuchiya, N., 2009. Direct measurement of contact area and stress dependence of anisotropic flow through rock fracture with heterogeneous aperture distribution. Earth Planet. Sci. Lett. 281 (1–2), 81–87.

Nick, K.E., Conway, M.W., Fowler, K.S., 1995. The relation of diagnetic clays and sulfates to the treatment of coalbed methane reservoirs. Paper SPE 30736 Presented at the SPE Annual Technical Conference and Exhibition, Dallas, Texas, October, 22–25. Society of Petroleum Engineers, Richardson, TX, p. 11.

Palmer, I., Mansoori, J., 1998. Permeability depends on stress and pore pressure in coalbeds, a new model. SPE Reserv. Eval. Eng. 1 (6), 539–544.

Pan, Z., Connell, L.D., Camilleri, M., 2010. Laboratory characterisation of coal reservoir permeability for primary and enhanced coalbed methane recovery. Int. J. Coal Geol. 82 (3–4), 252–261.

Pattison, C.I., Fielding, C.R., McWatters, R.H., Hamilton, L.H., 1996. Nature and origin of fractures in Permian coals from the Bowen basin, Queensland, Australia. In: Gayer, et al. (Eds.), Coalbed Methane and Coal Geology. London, Geological Society Special Publication, 109, pp. 131–150.

Polak, A., Elsworth, D., Yasuhara, H., Grader, A.S., Halleck, P.M., 2003. Permeability reduction of a natural fracture under net dissolution by hydrothermal fluids. Geophys. Res. Lett. 30 (20), 1–4.

Popp, T., Kern, H., 2000. Monitoring the state of microfracturing in rock salt during deformation combined measurements of permeability and P- and S-wave velocities. Phys. Chem. Earth Solid Earth Geod. 25 (2), 149–154.

Remeysen, K., Swennen, R., 2006. Beam hardening artifact reduction in microfocus computed tomography for improved quantitative coal characterization. Int. J. Coal Geol. 67 (1–2), 101–111.

Rowland, J.C., Manga, M., Rose, T.P., 2008. The influence of poorly interconnected fault zone flow paths on spring geochemistry. Geofluids 8, 93–101.

Song, D., Wang, E., Liu, J., 2012. Relationship between EMR and dissipated energy of coal rock mass during cyclic loading process. Saf. Sci. 50 (4), 751–760.

Stach, E., Mackowsky, M.T.H., Teichmueller, M., Taylor, G.H., Chandra, D.R., 1982. Coal Petrology. Gebruder Borntraeger, Stuttgart-Berlin 5–86.

Vinegar, H.J., Wellington, S.J., 1987. Tomographic imaging of three-phase flow experiments. Rev. Sci. Instrum. 58 (1), 96–107.

Vinokurova, E.B., 1978. The significance of sorption studies for practical coal mining. Solid Fuel Chem. 12 (6), 132–139.

Vishal, V., Ranjith, P.G., Singh, T.N., 2013. CO_2 permeability of Indian bituminous coals: implications for carbon sequestration. Int. J. Coal Geol. 105, 36–47.

Wang, S., Elsworth, D., Liu, J., 2011. Permeability evolution in fractured coal: the roles of fracture geometry and water-content. Int. J. Coal Geol. 87 (1), 13–25.

Wang, S., Elsworth, D., Liu, J., 2013. Permeability evolution during progressive deformation of intact coal and implications for instability in underground coal seams. Int. J. Rock Mech. Min. Sci. 58, 34–45.

Watanabe, N., Hirano, N., Tsuchiya, N., 2008. Determination of aperture structure and fluid flow in a rock fracture by high-resolution numerical modeling on the basis of a flow-through experiment under confining pressure. Water Resour. Res. 44 (6), 1–11.

Watanabe, N., Ishibashi, T., Hirano, N., Tsuchiya, N., Ohsaki, Y., Tamagawa, T., Tsuchiya, Y., Okabe, H., 2011a. Precise 3D numerical modeling of fracture flow coupled with X-ray computed tomography for reservoir core samples. SPE J. 16 (3), 683–690.

Watanabe, N., Ishibashi, T., Ohsaki, Y., Tsuchiya, Y., Tamagawa, T., Hirano, O., Okabe, H., Tsuchiya, N., 2011b. X-ray CT based numerical analysis of fracture flow for core samples under various confining pressures. Eng. Geol. 123 (4), 338–346.

Wolf, K.-H.A.A., Codreanu, D.B., Ephraim, R., Siemons, N., 2004. Analysing cleat angles in coal seams using image analysis techniques on artificial drilling cuttings and prepared coal blocks. Geol. Belg. 7 (3–4), 105–114.

Wolf, K.-H.A.A., van Bergen, F., Ephraim, R., Pagnier, H., 2008. Determination of the cleat angle distribution of the RECOPOL coal seams, using CT-scans and image analysis on drilling cuttings and coal blocks. Int. J. Coal Geol. 73 (3–4), 259–272.

Wu, Y., Chen, J., Zeng, S., 2011. The acoustic emission technique research on dynamic damage characteristics of the coal rock. Procedia Eng. 26, 1076–1082.

Yao, Y., Liu, D., Che, Y., Tang, D., Tang, S., Huang, W., 2009. Non-destructive characterization of coal samples from China using microfocus X-ray computed tomography. Int. J. Coal Geol. 80 (2), 113–123.

Yao, Y., Liu, D., Cai, Y., Li, J., 2010. Advanced characterization of pores and fractures in coals by nuclear magnetic resonance and X-ray computed tomography. Sci. China Earth Sci. 53 (6), 854–862.

Yu, Y., Zhang, H., Zhang, C., Hao, Z., Wang, L., 2013. Effects of temperature and stress on permeability of standard coal briquette specimen. J. China Coal Soc. 38 (6), 936–941 (in Chinese with an English abstract).

Zhao, Q., Hao, S., 2006. Anisotropy test instance of ultrasonic velocity and attenuation of coal sample. Prog. Geophys. 21 (2), 531–534 (in Chinese with an English abstract).

Zhao, Y., Jiang, Y., 2010. Acoustic emission and thermal infrared precursors associated with bump-prone coal failure. Int. J. Coal Geol. 83 (1), 11–20.

Zhou, F., 2012. Experiment of influence of fractures on coal/rock acoustic velocity: with Carboniferous seams of Qinshui basin as example. Coal Geol. Explor. 40 (2), 71–74 (in Chinese with an English abstract).

Zhu, W.C., Liu, J., Elsworth, D., Polak, A., Grader, A., Sheng, J.C., Liu, J.X., 2007. Tracer transport in a fractured chalk: X-ray CT characterization and digital-image-based (DIB) simulation. Transp. Porous Media 70 (1), 25–42.